Science & Technology Development Journal 2025, 28(3):3833-3839

Open Access Full Text Article

Research Article

Construction of $SrTiO_3$/g-C_3N_4 Heterojunction for Improved Visible-Light-Driven Photocatalytic Activity toward Decomposition of Organic Pollutants in Water

Ton Nu Quynh Trang[1,2], Nguyen Tran Giao Bao[1,2], Vu Thi Hanh Thu[1,2,*]

ABSTRACT

Photocatalyst-assisted artificial photosynthesis has been widely recognized as a promising approach for environmental treatment. In this work, a novel hydrothermal technique was employed to synthesize three-dimensional (3D) $SrTiO_3$, which was then combined with two-dimensional (2D) g-C_3N_4 via a self-assembly process to create a 2D/3D g-C_3N_4/$SrTiO_3$ heterojunction. The morphological characteristics and optical features of the fabricated photocatalysts were assessed using powder XRD, SEM, TEM, and UV-DRS spectroscopy. The photocatalytic activity of the obtained specimens was evaluated by monitoring the photodecomposition of methylene blue (MB), a persistent organic dye pollutant commonly found in wastewater, under visible light. The results demonstrated that the binary g-C_3N_4/$SrTiO_3$ hybrid semiconductor exhibited excellent photocatalytic behavior, achieving a degradation efficiency of 72% after 60 min with reaction kinetics (0.018 min^{-1}), which was nearly 1.3 and 66.25 times higher than that of g-C_3N_4 and $SrTiO_3$, respectively. This enhancement is ascribed to the effective creation of heterojunctions between g-C_3N_4 and $SrTiO_3$, which facilitate improved charge separation and transfer, thereby promoting the degradation efficiency of organic pollutants. Additionally, the photocatalyst demonstrated excellent stability and reusability over four successive cycles. Based on experimental observations, a plausible photocatalytic mechanism was proposed. These findings provide a promising route for designing efficient and durable photocatalytic materials for environmental applications.

Key words: g-C3N4, dye degradation, SrTiO3 nanocubes, heterogeneous structure, visible-light photocatalysis

[1]*Faculty of Physics and Physics Engineering, University of Science, Ho Chi Minh City, Vietnam*

[2]*Vietnam National University, Ho Chi Minh City, Vietnam*

Correspondence

Vu Thi Hanh Thu, Faculty of Physics and Physics Engineering, University of Science, Ho Chi Minh City, Vietnam

Vietnam National University, Ho Chi Minh City, Vietnam

Email: vththu@hcmus.edu.vn

History

- Received: 18-04-2025
- Accepted: 21-06-2025
- Published Online: 22-09-2025

DOI :

https://doi.org/10.32508/stdj.v28i3.4465

INTRODUCTION

In recent decades, growing concerns over environmental degradation and the demand for sustainable energy sources have made these issues central to global discussions. As a result, the development of clean and efficient technologies has gained significant importance. Among various emerging green technologies, photocatalysis has attracted considerable attention as a promising approach to addressing growing challenges related to energy and environmental sustainability[1–3]. To design photocatalysts derived from abundant materials, several key challenges must be addressed: (1) many metal oxides possess large band gaps, hindering their capability to absorb visiblelight; (2) the band edge positions of various photocatalysts are often misaligned, making them unsuitable for effective photocatalytic activity; (3) the rapid recombination of photoinduced hole–electron pairs hinders the effective separation and transport within the semiconductors; and (4) catalytically active sites are difficult to access at the surface to facilitate photocatalytic reactions[4,5]. Given the complexity of these requirements, it is unlikely that a single material can fulfill all these functions simultaneously. Therefore, hybrid heterostructures, composed of complementary materials that individually address specific aspects of the photocatalytic process, have emerged as promising candidates for efficient photocatalyst systems[6,7]. Semiconductor heterostructures featuring staggered conduction and valence band (VB) alignments can facilitate the spatial separation of charge carriers by confining photogenerated electrons and holes in different material components[1,4,8]. These heterostructure constituents can be further engineered to improve the absorption efficiency for photocatalytic performance in practical applications. $SrTiO_3$ has garnered significant attention as a potential environmentally friendly photocatalyst due to its high photoelectron conversion efficiency, stable crystal structure, excellent thermal stability, and large dielectric constant. As a transition-metal oxide with a perovskite-type ABO_3 structure, where Sr and Ti occupy the A and B sites, respectively, $SrTiO_3$ typically adopts a highly symmetric

Cite this article : Nu Quynh Trang T, Tran Giao Bao N, Thi Hanh Thu V. **Construction of $SrTiO_3$/g-C_3N_4 Heterojunction for Improved Visible-Light-Driven Photocatalytic Activity toward Decomposition of Organic Pollutants in Water**. *Sci. Tech. Dev. J.* 2025; 28(3):3833-3839.

cubic form[9,10]. Its favorable electronic band structure, anisotropic crystal facets, and structural symmetry contribute to effective charge carrier separation and transport, making it one of the most extensively investigated photocatalysts for splitting water. Additional advantages include low cost and strong long-term stability[11,12]. However, the practical application of $SrTiO_3$ remains limited due to its large band gap, which restricts absorption to the visible region, and the high recombination rate of photoinduced charge carriers[13,14]. Currently, various approaches have been explored to improve the photocatalytic efficiency of $SrTiO_3$ [15,16]. Among these, the construction of heterojunction composite photocatalysts by integrating materials with well-aligned energy band structures is one of the most effective methods for enhancing charge separation. Heterostructured semiconductors composed of two or more semiconductor materials enable the strategic coupling of band energy levels, offering a promising route to significantly enhanced photocatalytic performance.

Graphitic carbon nitride (g-C_3N_4) is widely recognized as a material with efficient photocatalytic performance in response to visible light, owing to its facile synthesis, distinctive two-dimensional (2D) π-conjugated structure, low production cost, and suitable electronic band configuration. Recent developments have shown that g-C_3N_4 nanosheets (NSs), characterized by a defect-rich framework and nitrogen-bridged poly (tri-s-triazine) units, have applications across various fields. Additionally, g-C_3N_4 exhibits a strong capability to sensitize reactive oxygen species, enabling the generation of superoxide radicals for the photodegradation of organic pollutants[17]. Despite these advantages, bulk g-C_3N_4 suffers from several drawbacks, including poor visible light absorption, a low surface area, and rapid recombination of photoinduced hole–electron pairs[18,19]. These limitations hinder its photocatalytic efficiency. The 2D form of g-C_3N_4, however, addresses these challenges by offering a larger surface area, increased density of active sites, and reduced electron–hole recombination, which significantly improve its photocatalytic performance[20]. To address the limitations associated with individual photocatalysts, numerous strategies have been investigated, including the formation of heterojunction catalysts through semiconductor coupling, the construction of two-dimensional nanojunctions, and the deposition of co-catalyst particles on the surface of g-C_3N_4. Given the favorable alignment of the band edges between $SrTiO_3$ and g-C_3N_4, particularly their closely matched conduction band (CB)levels, which facilitate energetically favorable electron transfer, the integration of these two materials is anticipated to yield a highly efficient heterojunction system[21]. Moreover, establishing a well-engineered interface between semiconductor components is crucial for facilitating charge transfer (CT) and enhancing the overall photocatalytic performance of the heterostructure compared to the individual materials. Heterostructured semiconductors are composite systems composed of two or more semiconductors. By coupling semiconductors with appropriately aligned band structures, these heterojunctions can potentially show improved photocatalytic performance, primarily by promoting efficient charge separation and transfer, which can lead to enhanced generation of reactive oxygen species. For example, Ferreira et al. have reported the synthesis of g-C_3N_4/$SrTiO_3$ heterostructures by combining pre-synthesized $SrTiO_3$ with melamine, followed by thermal treatment at 550°C for 2 hours. The resulting materials were subjected to photodegradation under visible light irradiation[22]. Zhang et al. have demonstrated the uniform fabrication of cyano-functionalized g-C_3N_4 ultrathin nanolayers on $SrTiO_3$ nanotubes via a straightforward one-step gas–solid reaction. The resulting heterostructures were subsequently employed for photocatalytic hydrogen evolution and carbon dioxide reduction[23]. While the photocatalytic potential of g-C_3N_4/$SrTiO_3$ binary hybrids has been extensively explored over the past decade, the development of a simple approach to construct high-performance 3D $SrTiO_3$ nanocubes and 2D g-C_3N_4 nanosheets could advance sustainable photocatalysis in environmental applications.

In this study, a 3D $SrTiO_3$ structure was synthesized, and a novel 3D/2D g-C_3N_4/$SrTiO_3$ nanojunction was constructed by integrating 2D g-C_3N_4 with 3D $SrTiO_3$ to enhance and stabilize photocatalytic performance. In this configuration, 3D $SrTiO_3$ functions as a co-catalyst supported on 2D g-C_3N_4, forming a unique interfacial architecture. The 3D to 2D structural design increases the interfacial contact area between the two semiconductors, providing a large number of active sites for photocatalytic reactions. Additionally, the internal electric field generated at the heterojunction interface promotes the rapid migration of photogenerated charge carriers toward reaction sites, effectively suppressing electron–hole recombination. As expected, the optimized g-C_3N_4/$SrTiO_3$ composite exhibited excellent photodegradation performance and robust cycling stability under visible light, confirming the improved photocatalytic efficiency of the synergistic 2D/3D heterostructure.

EXPERIMENTAL SECTION

Chemicals and reagents — Urea ($CO(NH_2)_2$), ethanol absolute (CH_3CH_2OH), titanium dioxide (TiO_2), sodium hydroxide pellets (NaOH, 98%), and strontium hydroxide octahydrate ($Sr(OH)_2{\cdot}8H_2O$, 98%). Double-distilled water (D/W) was used throughout the experiments.

Synthesis of $SrTiO_3$ nanocubes

The $SrTiO_3$ nanocubes were prepared via a hydrothermal approach. Initially, 1 g of TiO_2 was mixed with 100 mL of 5 M NaOH solution and 3.5 g of $Sr(OH)_2{\cdot}8H_2O$ in a 200 mL beaker, and the mixture was stirred continuously for 60 minutes. The obtained suspension was transferred into an autoclave and heated at 130°C for 24 hours. The obtained white solid was then thoroughly rinsed with D/W, and subsequently dried in air at 60°C.

Fabrication of 2D g-C_3N_4 NSs

Bulk g-C_3N_4 NSs were synthesized via a thermal polymerization pathway. In this process, 10 g of urea was situated in a partially covered ceramic crucible, heated to 550°C at a controlled rate of 2°C/min, and held for 2 hours. After cooling to room temperature, bulk g-C_3N_4 was obtained. To exfoliate the material, 400 mg of the bulk g-C_3N_4 was dispersed in 200 mL of 0.5 M HCl and stirred for 24 hours. The solid product was separated by centrifugation, followed by removal of the supernatant. The collected precipitate was subsequently dried in an oven at 60°C.

Synthesis of g-C_3N_4/$SrTiO_3$ heterostructures

The $SrTiO_3$/g-C_3N_4 nanostructures were fabricated via an ultrasonic-assisted self-assembly approach. Initially, 0.08 g of 2D g-C_3N_4 was added to 50 mL of D/W, while 10 mg of $SrTiO_3$ nanocubes were dispersed in 30 mL of D/W. The two dispersions were then combined and subjected toultrasonic treatment for 2 hours to ensure homogeneous dispersion and promote interfacial contact. The sample was collected by centrifugation, thoroughly rinsed with water and ethanol, and dried at 80°C.

Photocatalytic pollutant degradation

The photocatalytic behavior of the synthesized samples was evaluated by decomposing MB under visible light irradiation. In a standard procedure, 0.025 g of the obtained photocatalyst was dispersed in 50 mL of an aqueous MB solution with a concentration of 10 mg/L. The suspension was placed in the dark for 60 minutes to ensure adsorption–desorption equilibrium. Following this, the mixture was irradiated using a xenon arc lamp. Aliquots of 3 mL were withdrawn at 10-minute intervals, and the MB concentration was evaluated using UV–Vis absorption spectroscopy.

Characterization of materials

The morphology of the obtained specimens was examined using field-emission scanning electron microscopy (FESEM, Hitachi S-4800) coupled with energy-dispersive spectroscopy (EDS) and transmission electron microscopy (TEM, JEOL 2100 F). The crystalline phases were identified through powder X-ray diffraction (XRD) analysis performed on a Bruker D8 Advance diffractometer utilizing CuKα radiation. Optical properties were assessed through UV–Vis diffuse reflectance spectroscopy (DRS) with a Shimadzu UV-760 spectrophotometer.

RESULTS

The surface morphology of the ultrathin g-C_3N_4 nanosheets and $SrTiO_3$ nanocubes was analyzed using SEM and TEM, as shown in Figure 1. Figure 1(a–d) reveals that the g-C_3N_4 exhibits a two-dimensional porous architecture composed of thin nanosheets, marked by pronounced wrinkling and layered stacking, attributable to the exfoliation and acid treatment processes. This structure demonstrates the successful formation of crystalline g-C_3N_4. In contrast, the $SrTiO_3$ samples display uniform nanocubes withwell-defined crystalline features, characterized by a nearly perfect cubic morphology and six symmetricfacets, as shown in Figure 1(d,e).

The morphology of the g-C_3N_4/$SrTiO_3$ heterostructure was examined. It consisted of nonuniformly distributed aggregates of g-C_3N_4 and $SrTiO_3$, with distinct domains of each component observable in both SEM and TEM image (Figure 2). Detailed inspection of Figure 1(a, b) indicates that the $SrTiO_3$ nanocubes are tightly bound to the g-C_3N_4 NSs. In these images, darker regions correspond to the $SrTiO_3$ phase, whereas brighter regions indicate the presence of g-C_3N_4. This interfacial arrangement facilitates efficient CT and decreases the migration distance, supporting the successful formation of a heterojunction between the two materials.

XRD analysis was conducted to assess the crystallinity of g-C_3N_4, $SrTiO_3$, and the g-C_3N_4/$SrTiO_3$ heterostructure (Figure 3). The XRD spectra of g-C_3N_4 (blue) contains a prominent peak at 27.4°, corresponding to the (002) plane in aromatic systems (JCPDS 87-1526)[24]. For the $SrTiO_3$ nanocubes (pink), distinctive diffraction peaks observed at 2θ

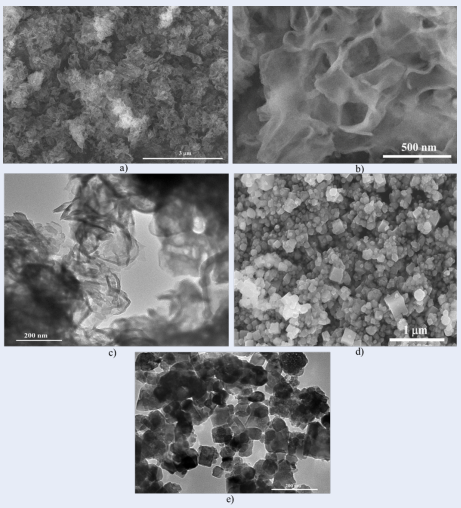

Figure 1: Characteristic morphologies of the obtained photocatalyst: (a,b) SEM, (c)TEM image of g-C_3N_4 NSs, (d) SEM, (e)TEM image of $SrTiO_3$

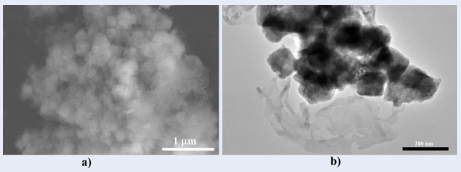

Figure 2: (a) SEM and (b) TEM image of g-C_3N_4/$SrTiO_3$ photocatalyst

values of 32.42°, 39.98°, 46.48°, 52.36°, and 57.79° were indexed to the (110), (111), (200), (210), and (211) crystal planes, respectively, matching the reference pattern (PDF#35–0734)[25]. The XRD profiles of the g-C_3N_4/$SrTiO_3$ heterostructure (green) exhibit diffraction peaks corresponding to both g-C_3N_4 and $SrTiO_3$, confirming the successful integration of the g-C_3N_4 and the $SrTiO_3$ nanocubes.

UV–vis DRS was conducted to evaluate the light absorption properties of the samples. As shown in Figure 4a, $SrTiO_3$ nanocubes exhibit a characteristic absorption edge around 380 nm. In contrast, g-C_3N_4 exhibits a broader visible light absorption range, with an absorption threshold of approximately 430 nm. In particular, the g-C_3N_4/$SrTiO_3$ composite exhibits a redshift in its absorption spectrum relative to the individual components, indicating a considerable enhancement in light-harvesting capability. These findings suggest that incorporating 2D g-C_3N_4 effectively extends the visible light response of the 3D SrTiO–based photocatalyst. The optical band gaps of the

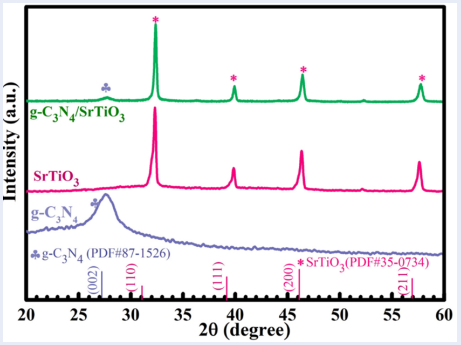

Figure 3: XRD patterns of the obtained samples

samples were further determined using the Tauc plot derived from the Kubelka–Munk function. As shown in Figure 4b, the corresponding band gap energy of 2D g-C_3N_4, 3D $SrTiO_3$, and 2D/3D g-C_3N_4/$SrTiO_3$ is approximately 2.9, 3.27, and 2.76 eV, respectively. Moreover, FTIR spectra were employed to further analyze the chemical structure of the synthesized photocatalysts, as shown in Figure 4c. All samples containing g-C_3N_4 exhibited similar characteristic peaks. The absorption band at 801 cm^{-1} corresponds to the out-of-plane bending vibration of the N–C=N units in the triazine rings. The peaks in the range of 1200–1700 cm^{-1} were attributed to the stretching vibrations of aromatic C–N heterocycles. A broad absorption band between 2900 and 3350 cm^{-1} was assigned to the residual -NH and -NH_2 groups from polymerization, as well as surface –OH groups from adsorbed H_2O molecules[26]. Furthermore, all $SrTiO_3$-based photocatalysts displayed distinct absorption bands near 448, 565, and 646 cm^{-1}, which can be attributed to the stretching vibrations of Sr–O, TiO_3^{2-}, and Ti–O bonds, respectively[27]. The characteristic peaks of $SrTiO_3$ remained after incorporation with g-C_3N_4, indicating that the structural framework of $SrTiO_3$ stayed intact following the loading of 2D g-C_3N_4 on the surface.

The photocatalytic efficacy of the obtained samples was investigated by examining the degradation of MB under visible light, as illustrated in Figure 5a. In the absence of a photocatalyst, minimal MB decomposition was observed even after 60 minutes of illumination, confirming that MB is not significantly affected by visible light alone. However, a marked increase in MB degradation occurred when catalysts were introduced under the same irradiation conditions. Among the tested materials, pure g-C_3N_4 exhibited moderate photocatalytic activity, achieving approximately 56% degradation after 50 minutes, which is attributed

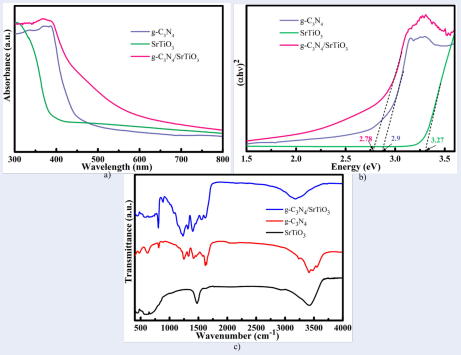

Figure 4: (a) UV-Vis DRS spectra, (b) bandgap energies and (c) FTIR spectra of samples

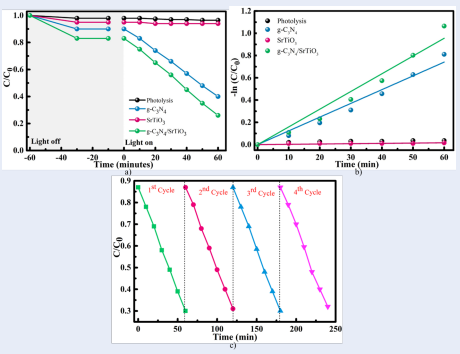

Figure 5: (a) Photocatalytic activity of MB degradation of samples, (b) plots of-ln (C_o/C) of the obtained samples, (c) The cycling experiments on the decomposition of MB by the g-C_3N_4/$SrTiO_3$ binary nanostructure

to limited charge carrier mobility. $SrTiO_3$ showed negligible activity due to its wide bandgap, which restricts visible light absorption. In contrast, the g-C_3N_4/$SrTiO_3$ composite exhibited significantly enhanced photocatalytic performance, with approximately 72% degradation of MB within 60 minutes, outperforming both its components. Kinetic analysis (Figure 5b) revealed that the degradation followed a pseudo-first order reaction model, with the g-C_3N_4/$SrTiO_3$ heterostructure demonstrating the highest apparent rate constant, 0.018 min^{-1}, approximately 1.3 and 66.25 times higher than those of g-C_3N_4 and $SrTiO_3$, respectively. This improved behavior is primarily assigned to the synergistic effect at the interface between g-C_3N_4 and $SrTiO_3$, which promotes effective charge separation and accelerates the migration of photoinduced electrons. Additionally, the composite benefits from extended visible light response and an increased surface area due to the layered structure of g-C_3N_4. The electrostatic interaction between the MB dye molecules and the g-C_3N_4 surface further improves adsorption. The composite offers more active sites, contributing to superior photocatalytic activity. The role of g-C_3N_4 in improving the photocatalytic behavior of $SrTiO_3$ is evident from these findings. Furthermore, the stability and recyclability of the g-C_3N_4/$SrTiO_3$ photocatalyst were assessed over four consecutive cycles (Figure 5c). After each cycle, the photocatalyst was collected by centrifugation, washed, dried, and reused. The results show that the composite retained its photocatalytic efficiency across all cycles, indicating excellent stability and reusability, which are essential for practical applications.

To investigate the role of photogenerated reactive species in the decomposition of MB, scavenger experiments were carried out using ethylenediaminetetraacetic acid disodium salt (EDTA-2Na) and benzoquinone (BQ) as selective quenchers for photoinduced holes (h^+) and superoxide radicals ($^{\bullet}O_2^-$), respectively[28]. As shown in Figure 6, the g-C_3N_4/$SrTiO_3$ photocatalyst achieved 72% decomposition of MB dye in the absence of any scavengers. When EDTA-2Na was introduced, no significant change in photocatalytic activity was observed, implying that while photoinduced holes (h^+) participate in the decomposition process, they are not the primary reactive species. In contrast, adding BQ suppressed the degradation efficiency to approximately 22%, suggesting that superoxide radicals ($^{\bullet}O_2^-$) are the dominant reactive species involved in the photocatalytic decomposition mechanism. The kinetics of the reaction under different scavenger conditions were further evaluated by determining the apparent rate constants (k), as shown in Figure 6b. Without the introduction of any scavengers, k for the 60-minute photocatalytic reaction was 1.065 min^{-1}. In the presence of BQ, k decreased to 0.2915 min^{-1}, further confirming that $^{\bullet}O_2^-$ species are the primary contributors to the photocatalytic activity of the g-C_3N_4/$SrTiO_3$ system.

DISCUSSION

Based on the above experimental outcomes, a plausible photocatalytic degradation mechanism is proposed, as shown in Figure 7. The CB energy (E_{CB}) and VB energy (E_{VB}) of g-C_3N_4 were −1.0 and 1.9 eV, respectively[29]. The E_{CB} and E_{VB} of $SrTiO_3$ were −0.89 eV and 2.38 eV, respectively[30]. Under visible light illumination, g-C_3N_4 is photoactivated, generating electron–hole pairs, while $SrTiO_3$ remains largely

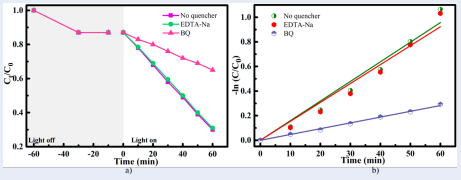

Figure 6: (a) Photocatalytic decomposition efficacy of MB with various scavengers.(b) Plots of rate constants ln C_o/C vs. time for the g-C_3N_4/$SrTiO_3$

inactive due to its relatively wide bandgap. The photoexcited electrons in the CB of g-C_3N_4 are transferred to the CB of $SrTiO_3$, where they subsequently react with dissolved oxygen molecules in the aqueous medium to form superoxide anion radicals ($^{\bullet}O_2^-$). Concurrently, the holes (h^+) retained in the VB of g-C_3N_4 do not effectively oxidize hydroxide ions or water to create hydroxyl radicals ($OH^{\bullet}$). Consequently, the $^{\bullet}OH$ species are not significantly generated, and the photoinduced h^+ directly participate in the oxidative degradation of the MB dye molecules. The proposed reaction pathway can be presented as the following sequence of photocatalytic reactions.

$$gC_3N_4/SrTiO_3 \xrightarrow{visible\ light} gC_3N_4(e^-/h^+)/SrTiO_3$$

$$gC_3N_4(e^-/h^+) + SrTiO_3 \xrightarrow{interfacial\ contact} gC_3N_4(h^+) + SrTiO_3(e^-)$$

$$SrTiO_3(e^-) + O_2 \rightarrow {\bullet}O_2^-$$

$${\bullet}O_2^-, h^+ + MB\ dye \xrightarrow{gC_3N_4} degraded\ products$$

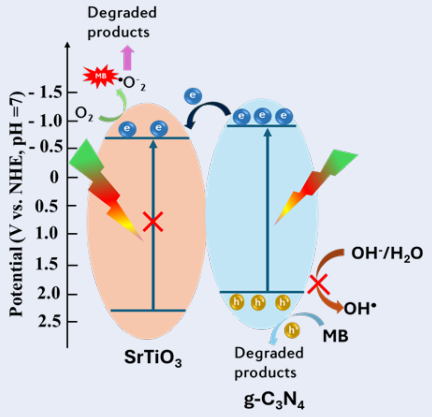

Figure 7: Photocatalytic reaction mechanism

CONCLUSIONS

In conclusion, a heterojunction photocatalyst for the decomposition of MB dye comprising 2D g-C_3N_4 and 3D $SrTiO_3$ has been successfully prepared. The 2D g-C_3N_4 nanosheets establish intimate interfacial contact with the 3D $SrTiO_3$ nanocubes, promoting efficient separation and transfer of photogenerated charge carriers. This synergistic interaction significantly enhances the photocatalytic performance by facilitating rapid charge migration while suppressing charge recombination. The g-C_3N_4/$SrTiO_3$ hybrid structure exhibits strong absorption in the visible light range and improved charge carrier dynamics, which are critical for high-efficiency photocatalysis. Under visible light illumination, the hybrid material exhibited a degradation efficiency of 72%, higher than that of pristine $SrTiO_3$ or g-C_3N_4. This study demonstrates a promising strategy for designing advanced heterostructured photocatalysts with enhanced charge separation capabilities for environmental applications.

COMPETING INTERESTS

The authors declare that there is no conflict of interest regarding the publication of this article.

AUTHORS' CONTRIBUTIONS

Ton Nu Quynh Trang has conceived of the present idea, carried out and written the manuscript with support from Vu Thi Hanh Thu

Nguyen Tran Gia Bao have done all experiments.

ABBREVIATIONS

NSs: nanosheets

CB: Conduction band

VB: Valance band

ACKNOWLEDGEMENTS

This research is funded by Vietnam National Foundation for Science and Technology Development (NAFOSTED) under grant number 103.03-2021.153.

REFERENCES

1. ARM R, JR A, V HJ, CR M, KE GP, S B, et al. Linker-Assisted Assembly of Ligand-Bridged CdS/MoS2 Heterostructures: Tunable Light-Harvesting Properties and Ligand-Dependent Control of Charge-Transfer Dynamics and Photocatalytic Hydrogen Evolution. ACS Appl Mater Interfaces. 2023;15:39966–39979.
2. TNQ T, NTG B, TT D, PT T, VTH T. Manipulating interface-induced multi-channel charge transfers toward highly hierarchical synchronous g-C3N4/STO@Pt modulation for boosting artificial photosynthesis. Int J Hydrogen Energy. 2024;74:346–360.
3. OF A. Photocatalytic water-splitting for hydrogen production using TiO 2 -based catalysts: Advances, current challenges, and future perspectives. Catalysis Reviews. 2025;1(38).

4. CR M, GE W, A F, DF W. Excited-State Charge Transfer and Extended Charge Separation within Covalently Tethered Type-II CdSe/CdTe Quantum Dot Heterostructures: Colloidal and Multilayered Systems. ACS Appl Mater Interfaces. 2021;13:30980–30991.
5. R B, KL B, TD K. Semiconductor nanocrystal photocatalysis for the production of solar fuels. J Chem Phys. 2021;154.
6. V HJ, and Rothfuss ARM ZW, CR M, G A, JL A, KE GP, et al. Lone but Not Alone: Precise Positioning of Lone Pairs for the Design of Photocatalytic Architectures. Chemistry of Materials. 2022;34:1439–1458.
7. ARM R, JR A, V HJ, CR M, KE GP, S B, et al. Linker-Assisted Assembly of Ligand-Bridged CdS/MoS2 Heterostructures: Tunable Light-Harvesting Properties and Ligand-Dependent Control of Charge-Transfer Dynamics and Photocatalytic Hydrogen Evolution. ACS Appl Mater Interfaces. 2023;15:39966–39979.
8. Q S, X Z, and Raza A LZ, G L. Plasmonic Au Nanoparticle of a Au/TiO2–C3N4 Heterojunction Boosts up Photooxidation of Benzyl Alcohol Using LED Light. ACS Appl Mater Interfaces. 2023;15:30161–30169.
9. B M, Q W, KT B, R GC, S S, A R, et al. Linking in situ charge accumulation to electronic structure in doped SrTiO3 reveals design principles for hydrogen-evolving photocatalysts. Nat Mater. 2021;20:511–517.
10. X L, FL-Y L, X H. Developing SrTiO3/TiO2 heterostructure nanotube array for photocatalytic fuel cells with improved efficiency and elucidating the effects of organic substrates. Chemical Engineering Journal. 2022;427:131602.
11. S P, V H, P R, P S, AAP KS, AM A. Tunable photocatalytic activity of SrTiO3 for water splitting: Strategies and future scenario. J Environ Chem Eng. 2020;8:103791.
12. H L, T H, Y G, M Y, T H, M K, et al. An Al-doped SrTiO3 photocatalyst maintaining sunlight-driven overall water splitting activity for over 1000 h of constant illumination. Chem Sci. 2019;10:3196–3201.
13. TNQ T, Van M T, TB P, VTH T. Spatially Controlled Photogenerated Charge Carriers Induced by SrTiO3 -Architectured Heterojunction Nanocubes for a Photocatalytic Hydrogen Evolution Reaction. ACS Appl Energy Mater. 2021;4:8910–8921.
14. Y J, J Z, X Z, Y M. Mechanistic insights into the role of empty mid-gap states in Al- and Rh-doped SrTiO3 for photocatalytic water splitting. Appl Surf Sci. 2025;694:162832.
15. Q W, Y Y, and Guo R PW. Sharing N atoms boosting Z-scheme charge transfer in SrTiO2 N/CNx heterojunctions for selective photoreduction of CO2 to CH4. Dalton Transactions. 2024;53:15048–15058.
16. K Z, Y-S F, L H, J M, M D, M-H X, et al. In-depth understanding of the band alignment and interface states scenario in Bi2O2Se/SrTiO3 ultrathin heterojunction. Rare Metals. 2025;44:1204–1212.
17. and Ma F XW, and Wang A LZ, M L, J H, G W, W T. Edge effect-modulated exciton dissociation and charge transfer in porous ultrathin tubular graphitic carbon nitride for boosting photoredox activity. J Mater Chem A Mater. 202210;10:18333–18342.
18. D M, and Zou Y ZZ, J C, J-W S. The progress of g-C3N4 in photocatalytic H2 evolution: From fabrication to modification. Coord Chem Rev. 2024;500:215489.
19. H Z, Y L, Y H, J Z, J Z, B H, et al. Cd-doped g-C3N4/Ag2S/Ag Z-scheme heterojunction for efficient photocatalytic hydrogen evolution. Fuel. 2025;389:134549.
20. Q C, J H, D C, L C, X L, Y S, et al. Fast charge transfer on NiS modified type-II heterojunction CdS/g-C3N4 driven by work function difference for improved photocatalytic hydrogen evolution. Int J Hydrogen Energy. 2025;105.
21. and Bai L ZZ, and Qu Y LZ, L J. Review of strategies for the fabrication of heterojunctional nanocomposites as efficient visible-light catalysts by modulating excited electrons with appropriate thermodynamic energy. J Mater Chem A Mater. 2019;7:10879–10897.
22. MA F, da Silva GTST, OF L, VR M, C R, MJM P, et al. Fabrication of SrTiO3/g-C3N4 heterostructures for visible light-induced photocatalysis. Mater Sci Semicond Process. 2020;108:104887.
23. and Li Y ZW, L W, F Z, Y A, G S, P Z. In situ construction of cyano-modified g-C3N4 nanolayer-coated SrTiO3 nanotubes by gas-solid reaction for efficient photocatalytic solar fuel production. Chemical Engineering Journal. 2023;469:143817.
24. Y W, M F, J K, N C, YK K. Kinetic Evidence for Type-II Heterojunction and Z -Scheme Interactions in g-C3N4/TiO2 Nanotube-Based Photocatalysts in Photocatalytic Hydrogen Evolution. ACS Appl Energy Mater. 2023;6:5197–5206.
25. Y Z, C L, Y Z, J W, A L, PF-X C. Boosting light harvesting and charge separation over hollow double-shelled Ag@SrTiO3-TiO2 with Z-scheme heterostructure for highly efficient photocatalytic reduction of nitrate to N2. Chemical Engineering Journal. 2023;457:140992.
26. M H, H U, C H, M T, and Zhang Y PW, and Wang C LW. Enhanced Photocatalytic H2 Evolution Performance of the Type-II FeTPPCl/Porous g-C3N4 Heterojunction: Experimental and Density Functional Theory Studies. ACS Appl Mater Interfaces. 2023;.
27. G M, CI P, S P, A V, S V, MS A, et al. Silver-decorated SrTiO3 nanoparticles for high-performance supercapacitors and effective remediation of hazardous pollutants. Environ Geochem Health. 2024;46(96).
28. H F, Y D, and Pan Y CZ, L Y, T F, N W, et al. Designing Z-scheme In2O3@ZnIn2S4 core-shell heterojunctions for enhanced photocatalytic multi-pollutant removal. J Hazard Mater. 2024;463:132820.
29. T MS, KC B, S L, TT D, VH K, SH H, et al. Coordinatively unsaturated atomically dispersed Pt+2-N4 sites on hexagonal nanosheet structure of g-C3N4 for high-performance photocatalytic H2 production. Appl Catal B. 2023;337:122959.
30. and Li Y ZW, L W, F Z, Y A, G S, P Z. In situ construction of cyano-modified g-C3N4 nanolayer-coated SrTiO3 nanotubes by gas-solid reaction for efficient photocatalytic solar fuel production. Chemical Engineering Journal. 2023;469:143817.